

# We are IntechOpen, the world's leading publisher of Open Access books Built by scientists, for scientists

**4,800**

Open access books available

**122,000**

International authors and editors

**135M**

Downloads

Our authors are among the

**154**

Countries delivered to

**TOP 1%**

most cited scientists

**12.2%**

Contributors from top 500 universities



**WEB OF SCIENCE™**

Selection of our books indexed in the Book Citation Index  
in Web of Science™ Core Collection (BKCI)

Interested in publishing with us?  
Contact [book.department@intechopen.com](mailto:book.department@intechopen.com)

Numbers displayed above are based on latest data collected.

For more information visit [www.intechopen.com](http://www.intechopen.com)



# Wind Turbine Airfoil Boundary Layer Optimization Using Genetic Algorithm with 3D Rotational Augmentation

*Youjin Kim, Galih Bangga and Antonio Delgado*

## Abstract

The airfoil shape of horizontal axis wind turbine (HAWT) blade is optimized using genetic algorithm (GA). The algorithm is set to find the final airfoil shape with the highest gliding ratio (GR) and larger laminar boundary layer regime along the airfoil surface. The main aim is to find the best airfoil shape of higher lift coefficient with reduced drag in boundary layer from the reference airfoil shape. A 3D correction law is applied to model the effect of optimized airfoil in 3D rotational augmented situation. The thrust and power curves are generated by the blade element (BEM) and free vortex (FV) codes with 3D and loss correction. The higher power production is given when the wind turbine blades are designed using the optimized airfoil. This increment is thought to be made from the efficiency caused by the reduced separation bubbles from reduced turbulent boundary layer and 3D rotational augmentation. To validate its effectiveness in case of soiled condition, the aerodynamic parameters of airfoils are recalculated by enforcing the airfoil to undergo earlier transition, which models the leading edge roughness. The results indicate the soiled condition that does not affect the aerodynamic efficiency of the airfoil due to the positive effect of 3D rotation augmentation.

**Keywords:** optimization, genetic algorithm, airfoil, wind turbine blade, aerodynamics, rotational augmentation

## 1. Introduction

The purpose of optimization is to find optimal solutions in scientific or engineering problems. The optimization can also be applied to many wind turbine problems. According to different objectives, constraints, algorithms, tools, and models, various types of optimization solutions are possible. In literature, Jabaraj and Iniyar [1] mentioned optimization models in the wind conversion system with different modelings such as planning model, energy supply-demand model, and forecasting model in 2000. The computational optimization algorithm is mentioned by Baños [2] for solving problems in renewable energy. The artificial intelligence methods are used for forecasting wind speed and power by Lei [3]. The updated numerical

simulations and other technology trends are reported in 2013 by Miller [4]. The wind farm layout optimization is reviewed by Serrano González [5]. Mostly objective functions are the minimization of cost of energy, maximization of the power production, minimization of the blade mass, and so on [6–20]. The geometrical, aerodynamic, and physical aspects are to be researched when the constraints are in the field of turbine design. Especially if the blade section shape, called airfoil, is targeted for aerodynamic optimization, stochastic optimization is preferred than the gradient one due to the usefulness in shape randomness [21]. Among many stochastic methods, Evolutionary Computation (EC) is considered in this paper.

The biological concept that survives the fittest individual in the environment among the others is applied in EC [22]. GA, which is one of ECs, runs until it finds the fitness individual with the highest fittest level from the given objective function. It considers the individual solution candidate as the gene, which is the concept of reproduction unit of Mendel [23], and the individuals are exposed to different strategies of genetics to make another generation of the solution candidate pool. The reproduction strategy includes reproduction, crossover, and mutation [24]. The airfoil shapes within given upper and lower bounds make possible solution candidates. The algorithm runs for the fittest individual in objective function  $f(x) = \{GR + X_{tr}\}$ , which means the algorithm finds the airfoil with the highest Gliding Ratio (GR) and the latest transition point ( $X_{tr}$ ), in other words, larger laminar boundary layer regime on the airfoil surface. It finds the best airfoil of the highest lift coefficient (Cl) and lowest drag coefficient (Cd) in the generated airfoil candidate pool [25].

Two airfoils are compared to show their GR, Cl, Cd, and Power production in the wind turbine unit. As the algorithm is run with calculations of the airfoil in 2D, the correction law to consider the 3D effects and Rfoil software is applied [26, 27]. The 3D rotational effect of rotating machines has been found by many. The lift coefficient of the fan blade was found to be three times higher by Himmelskamp in [28]. The lift coefficient of a wind turbine blade was also found to be higher at the inboard sections of the blade by the experiments of Ronsten and Bruining [29, 30]. Later, correction laws for the 3D effect were tried by numerical investigations. The quasi-3D approaches by Hansen [31] and Snel [32, 33] led to the quasi-3D Navier-Stokes mode [34], which confirmed its validity by Shen and Soerensen [35].

As the rotation of the rotor was found to reduce separation and transition by the Coriolis force [35], the 3D correction terms are considered together with the optimized airfoil shape. By comparing the results corrected by the 3D correction law, the effect of optimized shape for higher GR and larger laminar boundary layer in lift coefficient and power production under 3D rotational effects can be deduced. The rotor Power and thrust curves show the combined effect of optimized airfoil on lifting efficiency in the blade unit by BEM theory [36] and FV method [37]. The thrust and power curve comparison leads us to see the effect of the blade lift efficiency increment caused by the optimized airfoil. Moreover, as the total power from the rotor is considered based on each section of blade annulus in BEM, the effects each 3D corrected aerodynamic parameter values of blade section with optimized airfoils are combined to contribute to the increase of power production. Moreover, lifting line of FV method, which calculates total external force and the lift of vortices strength, is also based on the lifting lines on the divided blade segments [37]. Its power calculation also reveals the gathered influence of increased efficiency of the optimized airfoil in sections of the blade.

The compensation for some missing correction laws in power calculations from BEM and FV codes with 3D correction law is possible with the code B-Go. The code B-Go is validated with experimental and computational results, which confirm its

reliability based on several correction terms, including tip loss correction, and flow conditions such as massive flow separation takes place [38].

Another realistic rotational situation of airfoil is soiled condition [39]. The leading edge of the airfoil is exposed to debris, dirt, soil, and pollution, and so on in the real situation. The Cl parameter of airfoils is calculated with forced transition. As this contamination is known to decrease the rated and maximum power [40], the roughness sensitivity of airfoil is of importance in the generation of new airfoil. As the contamination usually forces the transition of boundary layer to the leading edge of airfoil, this study made optimized and reference airfoils to have  $X_{tr} = 0.05$  on the suction side and  $X_{tr} = 0.1$  on the pressure side as it is recommended in the work of [41].

This chapter illustrates the results of the airfoil and design shape of turbine blade in Section 2, followed by the aerodynamic characteristics in Section 3. The power calculation of the turbine blade with optimized airfoil with corrected BEM and B-Go is shown in Section 4. The airfoil validity in soil condition is elaborated in Section 5. The summarization of the results and their interpretation are shown in Section 6.

## 2. Airfoil and blade design

The optimized airfoil called S809gx is generated with the settled GA algorithm at the Reynolds number ( $Re$ )  $10^6$  [25]. The reference airfoil and wind turbine are NREL Phase VI [42, 43]. The difference of thickness, maximum thickness, and maximum camber values are negligible, as shown in **Table 1** and **Figure 1**.

Because the optimized airfoil is found from the algorithm run to finish at the higher GR and larger  $X_{tr}$  point value at specific angle of attack (AOA) [25], airfoil S809gx shows to have 121% higher GR value, 168% larger laminar boundary layer region on the suction side of airfoil, and 125% larger laminar boundary layer on

	S809	S809gx
Thickness (%)	20.99	20.3
Max. thickness possible (%)	38.3	38.7
Max. camber (%)	0.99	0.87
Max. camber possible (%)	83.3	43.6

**Table 1.**  
Airfoil properties [25].

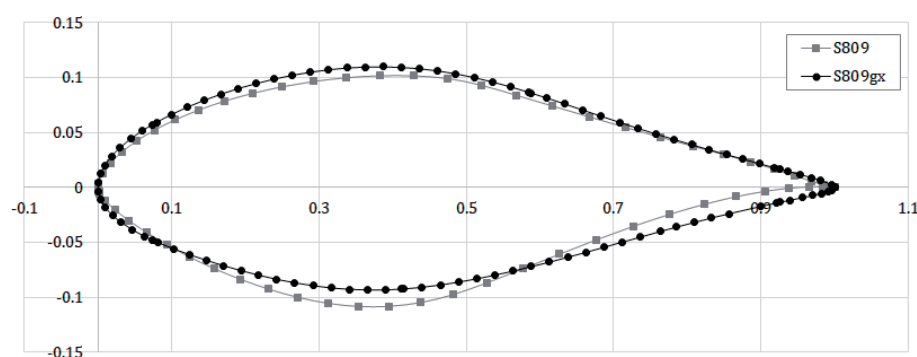


**Figure 1.**  
Optimized airfoil S809gx and reference S809 [25].

the pressure side at AOA  $7^\circ$ , as depicted in **Table 2**. It also indicates 140% higher GR values, 400% larger laminar boundary layer region on suction side, and 162% larger laminar boundary layer on the pressure side at AOA  $21.5^\circ$ . Those AOA values are chosen as the representative angle for fully attached and stall separation flow around airfoil.

The shape factor H of boundary layer [44] is plotted for both airfoils at targeted angle of attack. The optimized airfoil shows H values to be lower than 2.0 at  $x/c > 0.3$

	S809gx	S809	S809gx	S809
AOA ( $^\circ$ )	7	7	21.5	21.5
Cl	0.899	0.8793	1.0264	0.9149
Cd	0.011	0.0127	0.1566	0.1958
GR	85.29	69.50	6.553	4.672
Xtr (suction side)	0.272	0.162	0.016	0.004
Xtr (pressure side)	0.677	0.540	1.000	0.616

**Table 2.**  
GR and Xtr values of airfoils (Rfoil).

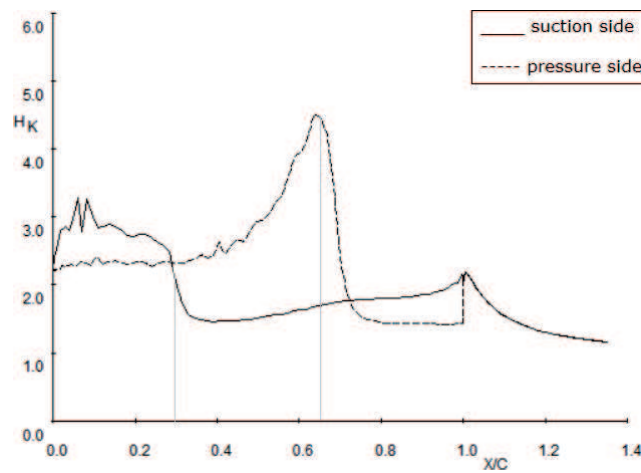


**Figure 2.**  
Shape factor of boundary layer of S809gx at AOA =  $7^\circ$ .

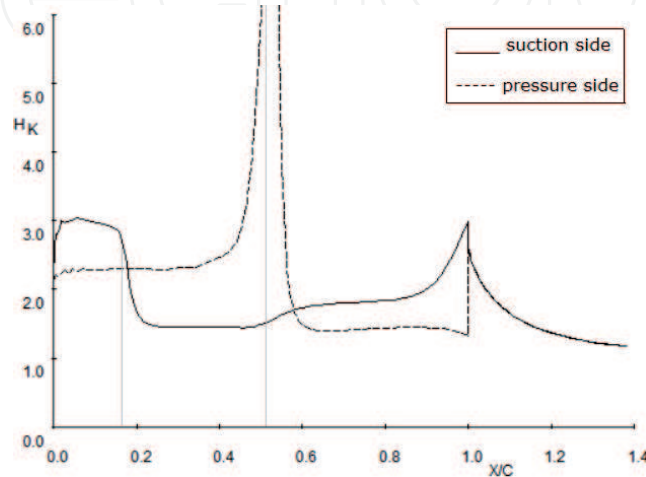


**Figure 3.**  
Shape factor of boundary layer of airfoil S809 at AOA =  $7^\circ$ .

when the reference airfoil shows drastically decreased H values at  $x/c \approx 0.2$ . The drag from turbulent boundary layer is expected more at the reference airfoil in the suction side.

Moreover, the trailing edge of S809 suction side also has separation with high H value, while S809gx has the smaller H value at the trailing edge. The pressure side transition is thought to be more violent at the S809 by the extremely different H values of transition point of pressure side of each airfoil, see **Figures 2 and 3**. In detail, it can be seen from **Figures 2 and 3**, that the shape factor of the airfoil drops significantly at  $x/c \approx 3$ , while it is much earlier for the reference airfoil at  $x/c \approx 0.18$ . This indicates delayed transition location, which confirms the previous discussion. Interestingly, the level of H for both airfoils within the laminar region is comparable at around  $H \approx 3.0$ , showing that the suction peak and its corresponding pressure gradient are comparable. A huge difference is observed on the pressure side when the transition occurs. Two main aspects can be seen: (1) transition occurs also at the delayed position at  $x/c \approx 0.65$  compared to the reference airfoil at  $x/c \approx 0.5$  and (2) the level of H at the location of transition is much smaller. The latter effect indicates that the laminar separation bubble is suppressed effectively for the optimized airfoil. This also indicates a reduced pressure gradient effect.

To check the validity of the optimized airfoil in soiled condition, boundary layer transition is forced to be 0.05 on the suction side and 0.1 on the pressure side, based on the roughness sensitivity experiment in [41], simulated in Rfoil for its 3D consideration [27].

Although GR values of airfoils are similar in different flow regimes in **Table 3**, the optimized one shows to have larger laminar boundary layer region over different AOA ranges in the forced transition situation, see **Figure 4**.

	S809gx	S809	S809gx	S809
AOA (°)	7	7	21.5	21.5
GR	61	61	7.53	6.67
Xtr (suction side)	0.05	0.05	0.0135	0.0025
Xtr (pressure side)	0.1	0.1	0.1	0.1

**Table 3.**  
 GR and Xtr values of airfoils with forced transition (Rfoil).

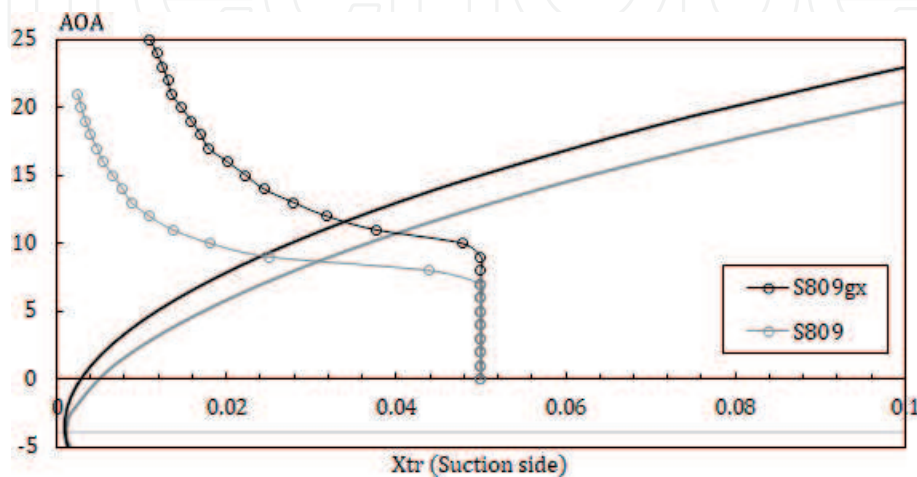


**Figure 4.**  
 Transition point ( $X_{tr}$ ) over angle of attack.

**Figure 2** shows the leading edge of airfoil as background of the graph. The airfoil S809gx has the larger laminar boundary layer region over all angle of attack values. It indicates that the optimized airfoil is shaped to have larger laminar boundary layer region even after transition is forced to be earlier than the normal state. Based on the assumption that the soiled condition triggers earlier boundary layer transition that occurs earlier than clean air condition [41], the optimized S809gx airfoil can be also useful under real air contamination situation [39], which will be discussed further in Section 5.

The wind turbine blade design with the optimized airfoil and the reference one is compared in **Figures 5** and **6**. The blade is designed with the same twist angle and chord length distribution based on Ref. [42], and the only difference is the airfoil type.

The blades designed with each airfoil are visualized in **Figures 5** and **6**. The airfoil distribution along the radial position with chord length distribution is based on the NREL Phase VI design guidelines [42], see **Tables 4** and **5**.

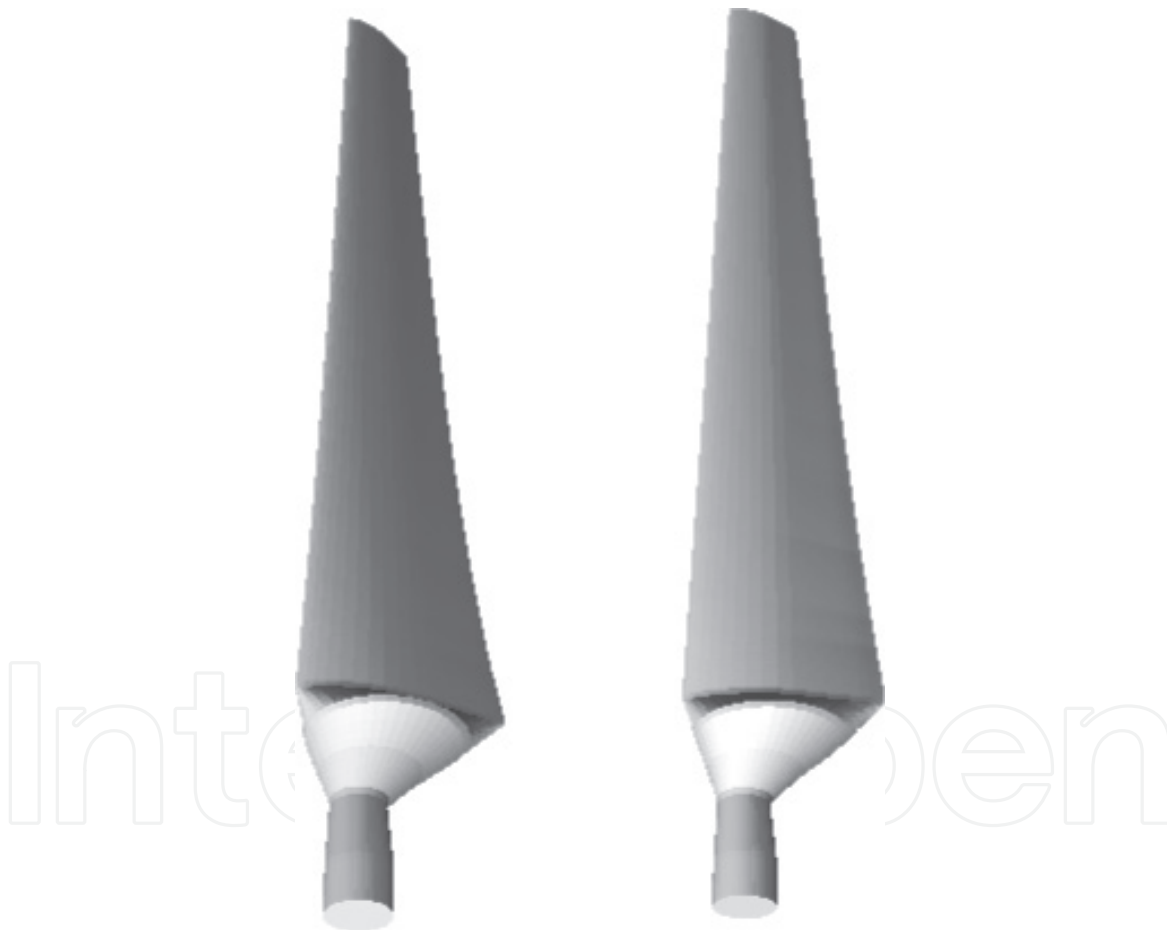


**Figure 5.**  
*Blade designed with the airfoil S809gx (left) and the airfoil S809 (right).*



**Figure 6.**  
*Top view of the blade with S809gx (left) and S809 (right).*

Radial position (m)	Chord length (m)	Twist (°)	Airfoil
0.508	0.218	0	Circular
0.66	0.218	0	Circular
0.883	0.183	0	Circular
1.008	0.349	0	Circular
1.067	0.441	0	Circular
1.133	0.544	0	Circular
1.257	0.737	20.04	S809
1.343	0.728	18.07	S809
1.51	0.711	14.29	S809
1.648	0.697	11.91	S809
1.952	0.666	7.98	S809
2.257	0.636	5.31	S809
2.343	0.627	4.71	S809
2.562	0.605	3.42	S809
2.867	0.574	2.08	S809
3.172	0.543	1.15	S809
3.185	0.542	1.115	S809
3.476	0.512	0.494	S809
3.781	0.482	-0.015	S809
4.023	0.457	-0.381	S809
4.086	0.451	-0.475	S809
4.391	0.42	-0.92	S809
4.696	0.389	-1.352	S809
4.78	0.381	-1.469	S809
5	0.358	-1.775	S809

**Table 4.**  
 Blade property of NREL Phase VI.

Radial position (m)	Chord length (m)	Twist (°)	Airfoil name
0.508	0.218	-3.00	Circular
0.660	0.218	-3.00	Circular
0.883	0.183	-3.00	Circular
1.008	0.349	-3.00	Circular
1.067	0.441	-3.00	Circular
1.133	0.544	-3.00	Circular
1.257	0.737	17.04	s809gx
1.343	0.728	15.07	s809gx
1.510	0.711	11.29	s809gx
1.648	0.697	8.91	s809gx
1.952	0.666	4.98	s809gx
2.257	0.636	2.31	s809gx



Radial position (m)	Chord length (m)	Twist (°)	Airfoil name
2.343	0.627	1.71	s809gx
2.562	0.605	0.42	s809gx
2.867	0.574	-0.92	s809gx
3.172	0.543	-1.85	s809gx
3.185	0.542	-1.89	s809gx
3.476	0.512	-2.51	s809gx
3.781	0.482	-3.02	s809gx
4.023	0.457	-3.38	s809gx
4.086	0.451	-3.475	s809gx
4.391	0.420	-3.92	s809gx
4.696	0.389	-4.35	s809gx
4.780	0.381	-4.47	s809gx
5.000	0.358	-4.78	s809gx

**Table 5.**  
Airfoil S809gx distribution along the blade.

### 3. Aerodynamic parameters

Regarding the aerodynamic parameters like Cl, Cd, and GR, two airfoils show similar distribution over the angles of attack. However, the optimized airfoil indicates slightly increased Cl and decreased Cd. Those small advantageous differences are summed up to show increased GR.

The Cl values are corrected with the 3D correction law, mainly considering twist angle and chord per radius ratio of the blade in turbine unit. The corrected value conveys the effect of the Coriolis, centrifugal force, delay of separation, and so on in rotational augmentation [32, 33]. As the rotational effect is significant in lift force, the correction law is only applied in Cl, not Cd. The reference experiments are found in the works of [45, 46]. The calculations are done in  $Re=10^6$ .

The optimized airfoil Cl values show slightly advantageous over stall angle of attack region compared to the reference one, see **Figure 7**. The drag coefficient is also smaller than the reference, as shown in **Figure 8**. Although the airfoil was designed to have better GR value by 2D calculation at the target of angle of attack of  $7^\circ$ ,

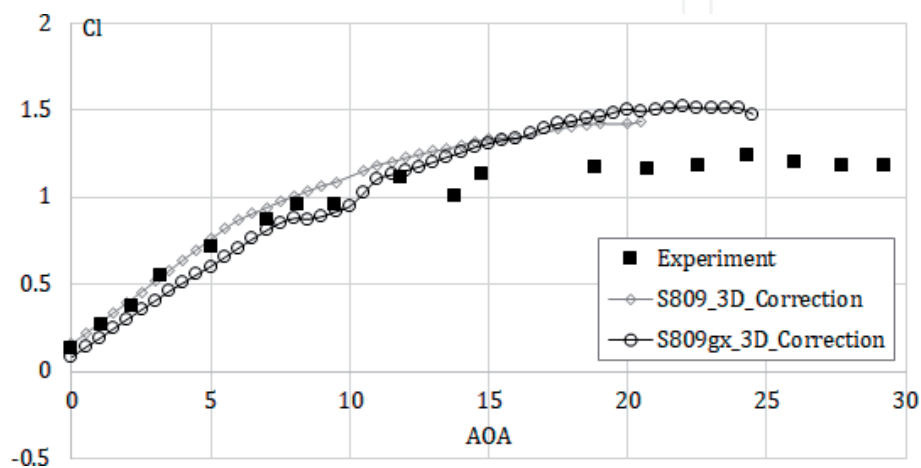


**Figure 7.**  
Cl distribution over angle of attack (°).

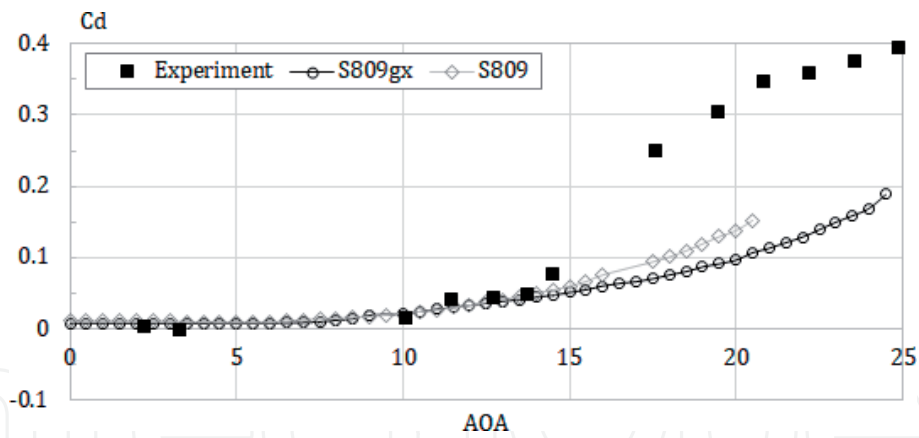


Figure 8.  
*Cd* distribution over angle of attack ( $^{\circ}$ ).

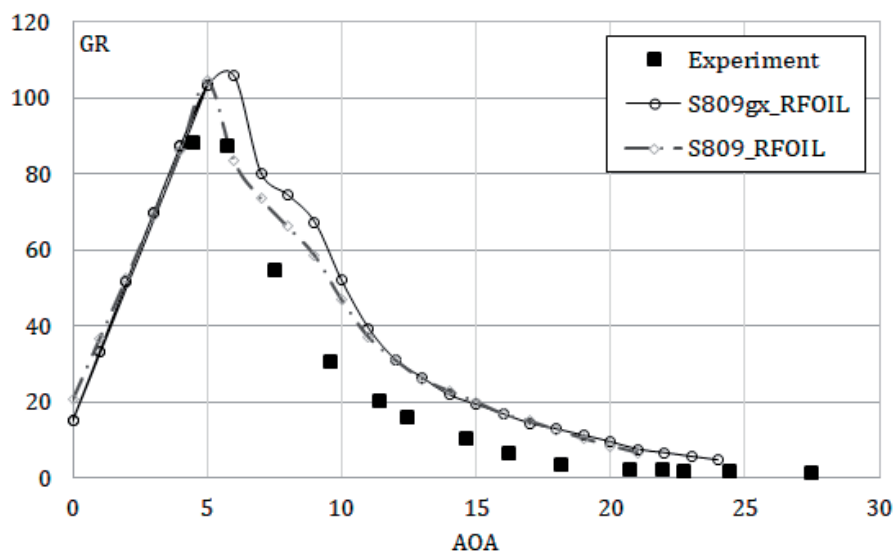


Figure 9.  
*GR* vs. *AOA* ( $^{\circ}$ ).

the 3D corrected value also shows the advantage of airfoil S809gx over the different angle of attack ranges.

Cl values corrected by 3D correction law of Hansen [31] in **Figure 7** are also supported by the GR calculation of software Rfoil, which improves the 2D prediction with the treated laminar and turbulent boundary layer closure problems [47, 48] in **Figure 9**. Based on the Rfoil validity [27], increased GR values of the airfoil S809gx especially at fully attached angle of attack range (5–13°) show positive implication for improvement of the following power production in the wind turbine unit.

#### 4. Thrust and power curves

To run the code simulation for reference turbine and turbine with optimized airfoil, operation properties are set as **Table 6**. A fixed pitch value of  $3^{\circ}$  (equal to turbine 1) is controlled in blade distribution property in **Table 5** for turbine 2. Blade 1 is designed with the reference airfoil S809 [42], and blade 2 is designed with the optimized airfoil S809gx.

Although the advantage of the optimized airfoil in Cl, Cd, and GR values seems to be negligible in **Figures 7–9**, power production curve shows how blade lift efficiency is improved by those airfoil construction, as shown in **Figure 10**. The thrust

	Turbine 1	Turbine 2
Power regulation	Stall	Stall
Transmission	Single	Single
V cut in (m/s)	6.00	6.00
V cut out (m/s)	25.00	25.00
Rotational speed (rpm)	71.63	71.63
Outer radius (mm)	5000.00	5000.00
Fixed pitch (°)	3.00	0.00
Variable losses	0.22	0.22
Blade type	Blade 1	Blade 2

**Table 6.**  
Properties for turbines [42].

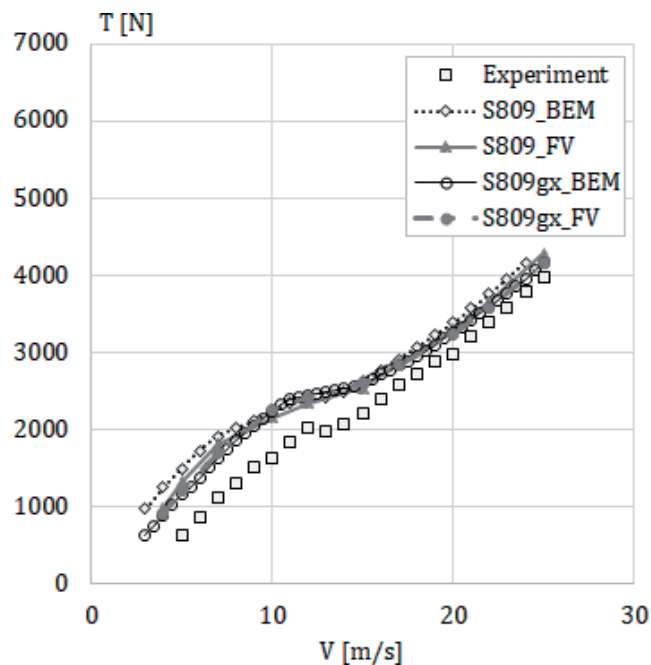


**Figure 10.**  
Power-velocity curve.

forces are calculated to show the values that are similar at blades with both airfoils, see **Figure 11**. The similarity in value distribution of thrust implies the power increment that is caused by increased lift velocity from the blade designed with the optimized airfoil.

As the Power Production is calculated by all lifting efficiencies of each blade section [48], combined advantage of each section of blade airfoil produces largely increased power production simulation, especially in the inflow velocity range of 7–25 m/s. Considering the discrepancies between different tools of calculation, the optimized airfoil turbine produced 150% larger power than the reference one. As the optimized airfoil turbine power prediction is based on the simulation of reference one, validated with its experimental data, the discrepancy between experimental data and calculation in high velocity (15–25 m/s) should be considered more.

The thrust curves show similar value pattern with B-Go code, except the fact that thrust force is estimated to be higher at the velocity of flow stall regime, where the prediction can be misled in BEM and FV codes [38]. The B-Go code thrust

calculation also supports the increment in blade velocity with the optimized airfoil as the thrust is not increased drastically in the turbine blade designed with the S809gx, see **Figure 12**.

The power value validation in high velocity, which would cause stall delay in blade [33], is tried with the state-of-the-art-code B-Go. The B-Go has been coded with the off design flow region where separation frequently occurs to make BEM code to be

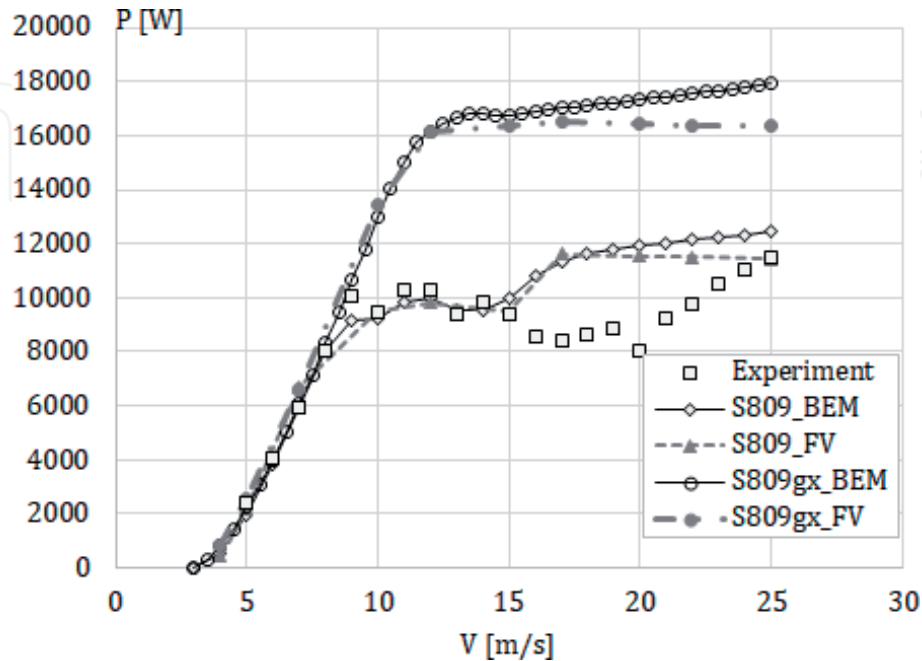


**Figure 11.**  
*Thrust-velocity curve.*

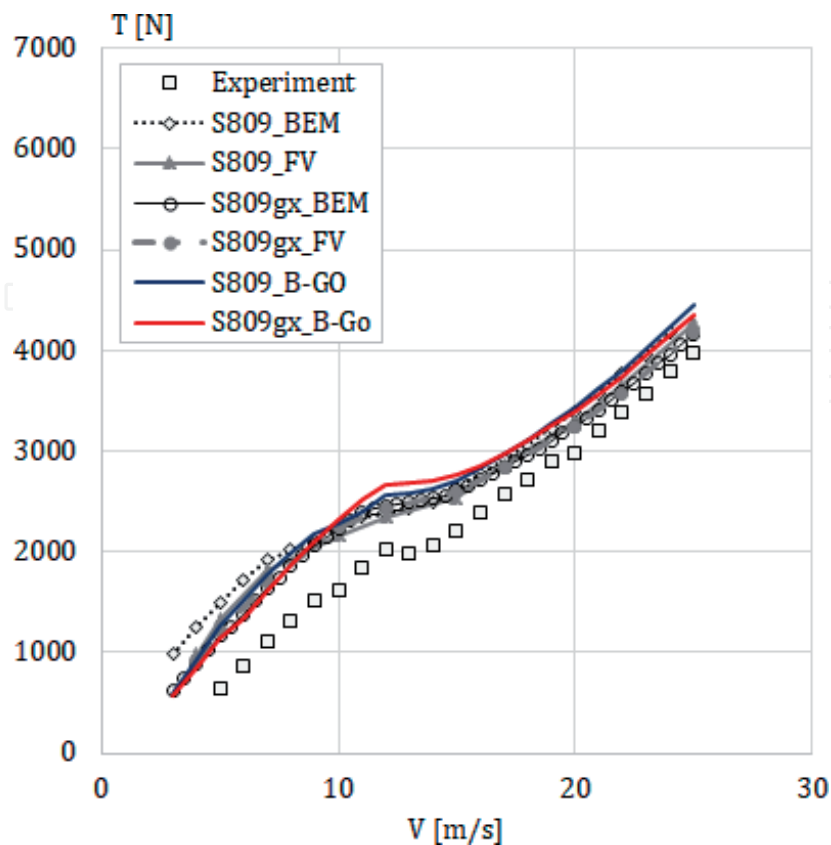


**Figure 12.**  
*Thrust-velocity curve with B-GO code.*

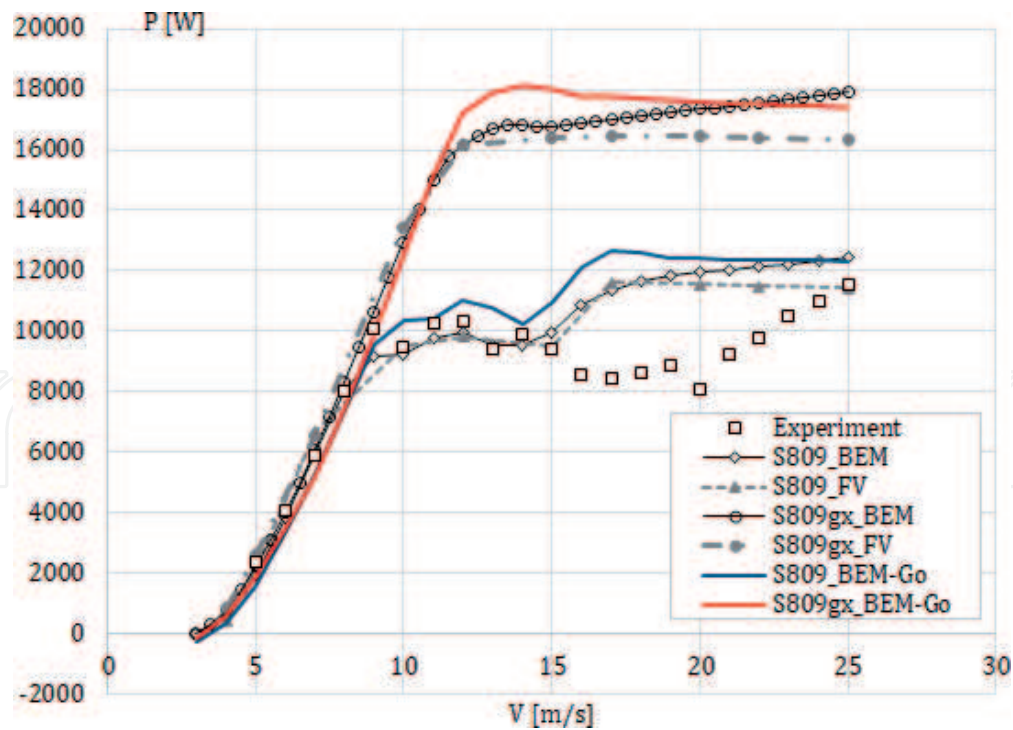


**Figure 13.**  
Power-velocity curve with B-GO code.

challenged in prediction [38], the power values at high velocity are predicted in spite of the discrepancy with experimental data. Although BEM and FV calculations show the value gap in the velocity of 15–25 m/s region, the B-GO codes show the similar pattern with the other codes. The increasing power values in stall region by BEM prediction show the weakness of BEM at the stall region [37, 38]. It also implies the possibility, which experimental data might have had the error in the stall region, as the experimental set up also has their limit in stall region measurements. The optimized airfoil turbine shows c.a. 150% higher power production in stall region, see **Figure 13**.

## 5. Performance of the optimized airfoil under soiled condition

As it is shown in Section 2, the optimized airfoil shape shows larger laminar boundary layer regimes even under a forced transition situation, which imitates the soiled condition, as shown in **Figure 4**. Not only smaller drag within the boundary layer but also the lift coefficient at the forced transition is benefitted because of the enlarged laminar boundary region at optimized airfoil. As it is shown in **Figure 14**, the  $C_l$  value difference of optimized airfoil at forced transition and normal transition situation is negligible. The influence of difference of  $C_l$  on GR, calculated by  $R_{foil}$ , is also demonstrated in **Figure 15**. The optimized airfoil is less sensitive to changes in inflow conditions. This is not only caused by its 2D characteristics but also being supported by the 3D rotational effects, which delays flow separation and reduces the turbulent boundary layer drag [32, 33]. The optimized airfoil can be tolerable in efficiency decrement in soiled condition or other causes of earlier transition occurrences.

## 6. Conclusions

Stochastic optimization, GA, has been applied to optimize airfoil shape toward larger GR and advantageous boundary layer transition in HAWT. The resulted

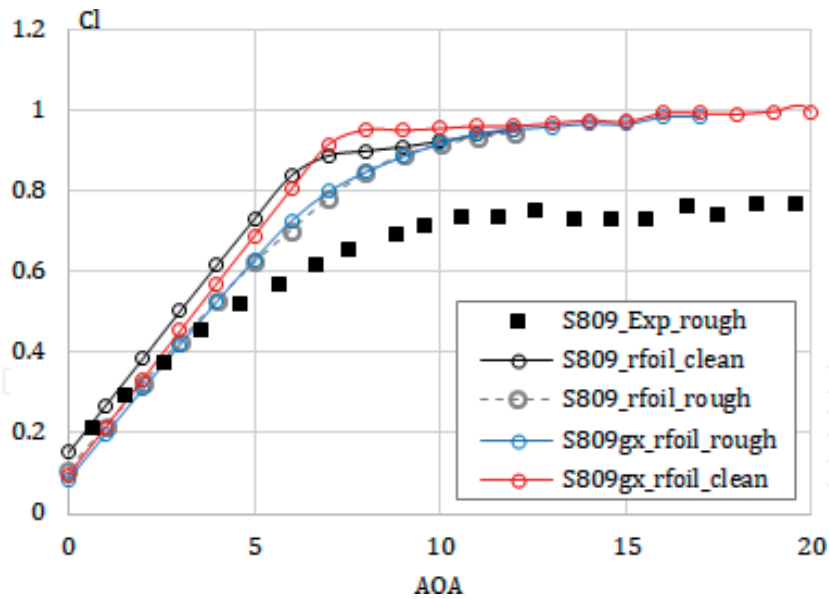


**Figure 14.**  
*Cl distribution at soil condition with experiment [49].*

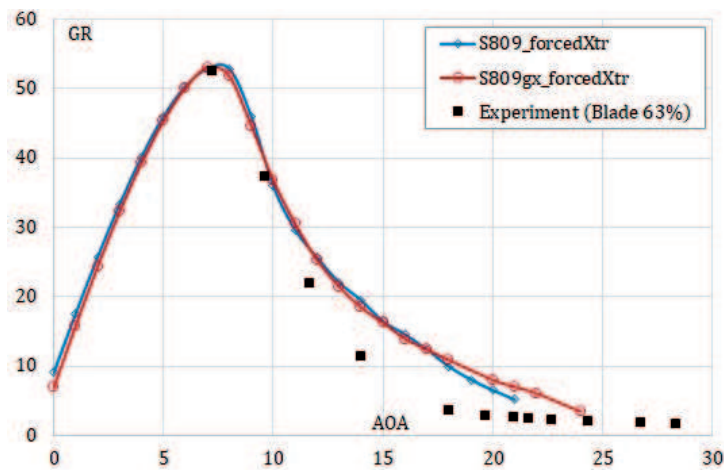


**Figure 15.**  
*GR comparison of airfoil in forced transition with experiment [42].*

airfoil shows a 121% higher GR, c.a. 120–170% larger laminar boundary layer on the airfoil surface in targeted AOA ( $^{\circ}$ ). The Cl, Cd, and GR values of two airfoils seem to be slight in the results; however, the power production predicted by different codes shows the combined effect of optimized airfoil rotor sections that lead to 150% higher power production. The thrust curves show a similar distribution pattern, indicating the velocity of the blade designed with optimized airfoil influences the power improvement, not the thrust force. The corrected BEM code with 3D rotational augmentation and B-Go codes for the stall region are used for compensating the prediction weakness of BEM in flow separation. The airfoil validity in soil condition is simulated with a forced transition, which shows a negligible lifting coefficient decrement in the optimized airfoil. The laminar boundary layer is still broader at optimized airfoil in forced transition, which indicates that the optimized airfoil shape is useful for realistic airflow with dirt and 3D rotation.

## Acknowledgements

Busan Brain 21 project of BMC is appreciated for its funding in this research.

IntechOpen

**Author details**

Youjin Kim<sup>1\*</sup>, Galih Bangga<sup>2</sup> and Antonio Delgado<sup>1</sup>


1 Institute of Fluid Mechanics, FAU Erlangen-Nürnberg, Erlangen, Germany

2 Institute of Aerodynamics and Gas Dynamics, University of Stuttgart, Stuttgart, Germany

\*Address all correspondence to: youjin.kim@fau.de

**IntechOpen**

---

© 2020 The Author(s). Licensee IntechOpen. Distributed under the terms of the Creative Commons Attribution - NonCommercial 4.0 License (<https://creativecommons.org/licenses/by-nc/4.0/>), which permits use, distribution and reproduction for non-commercial purposes, provided the original is properly cited. 

## References

- [1] Jebaraj S, Iniyan S. A review of energy models. *Renewable and Sustainable Energy Reviews*. 2006;**10**(4):281-311. DOI: 10.1016/j.rser.2004.09.004
- [2] Baños R, Manzano-Agugliaro F, Montoya F, Gil C, Alcayde A, Gómez J. Optimization methods applied to renewable and sustainable energy. *Renewable and Sustainable Energy Reviews*. 2011;**15**(4):1753-1766
- [3] Lei M, Shiyan L, Chuanwen J, Hongling L, Yan Z. A review on the forecasting of wind speed and generated power. *Renewable and Sustainable Energy Reviews*. 2009;**13**(4):915-920
- [4] Miller A, Chang B, Issa R, Chen G. Review of computer-aided numerical simulation in wind energy. *Renewable and Sustainable Energy Reviews*. 2013;**25**:122-134
- [5] Serrano González J, Burgos Payán M, Santos JMR, González-Longatt F. A review and recent developments in the optimal wind-turbine micro-siting problem. *Renewable and Sustainable Energy Reviews*. 2014;**30**:133-144
- [6] Fuglsang P, Aagaard Madsen H. Optimization of stall regulated rotors. In: *Proceedings of 1995 American Society of Mechanical Engineers (ASME) Energy Sources Technology Conference and Exhibition*. Houston, TX, United States; 1995
- [7] Fuglsang P, Aagaard Madsen H. *A Design Study of a 1 MW Stall Regulated Rotor*. Roskilde, Denmark: Risø National Laboratory; 1995
- [8] Fuglsang P, Bak C, Schepers J, Bulder B, Cockerill T, Claiden P, et al. Site specific design optimization of wind turbines of 1.5-2.0MW wind turbines. *Wind Energy*. 2002;**5**(4):261-279
- [9] Bak C. Aerodynamic design of wind turbine rotors. In: Brønsted P, Nijssen R, editors. *Advances in Wind Turbine Blade Design and Materials*. Sawston, Cambridge: Woodhead Publishing Limited; 2013. ISBN 978-1-84569-580-4
- [10] Ning A, Damiani R, Moriarty P. Objectives and constraints for wind turbine optimization. In: *31st ASME Wind Energy Symposium*. 2013
- [11] Fuglsang P, Madsen HA. Optimization method for wind turbine rotors. *Journal of Wind Engineering and Industrial Aerodynamics*. 1999;**80**:191-206
- [12] Xudong W, Shen WZ, Zhu WJ, Sorensen JN, Jin C. Shape optimization of wind turbine blades. *Wind Energy*. 2009;**12**:781-803
- [13] Maki K, Sbragio R, Vlahopoulos N. System design of a wind turbine using a multi-level optimization approach. *Renewable Energy*. 2012;**43**:101-110
- [14] Benini E, Toffolo A. Optimal design of horizontal-axis wind turbines using blade-element theory and evolutionary computation. *ASME Journal of Solar Energy Engineering*. 2002;**124**:357-363
- [15] Eke G, Onyewudiala J. Optimization of wind turbine blades using genetic algorithm. *Global Journal of Researches in Engineering*. 2010;**10**
- [16] Morgan C, Garrad A. The design of optimum rotors for horizontal axis wind turbines. In: *Proceedings of the 10th BWEA Wind Energy Conversion Conference*. London, England; 1988
- [17] Snel H. Review of aerodynamics for wind turbines. *Wind Energy*. 2003;**6**:203-211
- [18] Li JY, Li R, Gao Y, Huang J. Aerodynamic optimization of wind



turbine airfoils using response surface techniques. Proceedings of the Institution of Mechanical Engineering. 2010;**224**:827-838

[19] Liao CC, Zhao XL, Xu JZ. Blade layers optimization of wind turbines using FAST and improved PSO algorithm. *Renewable Energy*. 2012;**42**:227-233

[20] Wang L, Wang TG, Luo Y. Improved non-dominated sorting genetic algorithm (NSGA)-II in multi-objective optimization studies of wind turbine blades. *Applied Mathematics and Mechanics*. 2011;**32**:739. DOI: 10.1007/s10483-011-1453-x

[21] Chehour A, Younes R, Ilinca A, Perron J. Review of performance optimization techniques applied to wind turbines. *Applied Energy*. 2015;**142**:361-388

[22] Fogel DB. Introduction. In: Bäck T, Fogel DB, Michalewicz Z, editors. *Handbook of Evolutionary Computation*. San Francisco, California: Morgan Kaufmann Publisher; 1997. pp. 1-2. ISBN: 0750303921

[23] Windle BCA. Mendel and his theory of heredity. In: *A Century of Scientific Thought and Other Essays*. Burns & Oates; 1915

[24] King RC et al. *A Dictionary of Genetics*. 7th ed. Oxford, England: University Press; 2006. p. 129. ISBN: 978-0-19-530761-0

[25] Kim Y, Al-Abadi A, Delgado A. Airfoil Boundary Layer Optimization Toward Aerodynamic Efficiency of Wind Turbines: Chapter from the Book *Flight Physics—Models, Techniques and Technologies*

[26] Snel H, Houwink R, Bosschers J, Piers WJ, Bruining A. Sectional Prediction of 3-D Effects for Stalled Flows on Rotating Blades and

Comparison with Measurements: Proceedings of the ECWEC '93 Conference. Travemunde, Germany. pp. 395-399

[27] van Rooij, RPJOM. Modification of the Boundary Layer Calculation in RFOIL for Improved Airfoil Stall Prediction: Report IW-96087R, Delft University of Technology, Delft, The Netherlands. Available from: <http://www.windenergy.citg.tudelft.nl/>

[28] Himmelskamp H. Profile Investigation on a Rotating Airscrew, Technical Report [dissertation], Gottingen, Germany; 1945

[29] Ronsten G. Static Pressure Measurements on a Rotating and a Non-Rotating 2.375 m Wind Turbine Blade—Comparison with 2-D Calculations, Proceedings of the EWEC '91 Conference. Amsterdam; 1991. pp. 214-220

[30] Bruining A, Van Bussel GJW, Corten GP, Timmer WA. Pressure Distribution from a Wind Turbine Blade; Field Measurements Compared to 2-Dimensional Wind Tunnel Data, Technical Report IW-93065R. Delft University of Technology, Institute of Wind Energy; 1993

[31] Hansen MOL, Soerensen JN, Michelsen JA, Soerensen NN. A Global Navier-Stokes Rotor Prediction Model, 35th AIAA Aerospace Sciences Meeting & Exhibit. Reno: AIAA paper; 1997. pp. 97-0970

[32] Snel H, Houwink R, Piers WJ. Sectional Prediction of 3-D Effects for Separated Flow on Rotating Blades. Avignon, France: Eighteenth European Rotorcraft Forum; 1992

[33] Snel H, Houwink R, Bosschers J, Piers WJ, Bruining A. Sectional Prediction of 3-D Effects for Stalled Flows on Rotating Blades and Comparison with Measurements,

Proceedings of the ECWEC '93 Conference. Travemunde, Germany; 1993. pp. 395-399

[34] Soerensen DN, Soerensen JN. Quasi 3-dimensional model for rotating airfoil. In: 13th AIAA Applied Aerod Conference. San Diego, CA: AIAA; 1995. pp. 95-1916

[35] Shen WZ, Soerensen JN. Quasi-3D Navier-stokes model for rotating airfoil. *Journal of Computational Physics*. 1999;150:518-548

[36] Ingram G. Wind Turbine Blade Analysis Using the Blade Element Momentum Method Version 1.0. Durham, UK: School of Engineering, Durham University; 2005

[37] van Garrel A. Development of a wind turbine aerodynamics simulation module, ECN-C-03-079; 2003

[38] Bangga G. Comparison of blade element method and CFD simulations of a 10MW wind turbine. *Fluids*. 2018;3(4):73. DOI: 10.3390/fluids3040073

[39] van Rooij RPJOM, Timmer WA. Roughness Sensitivity Consideration for Thick Rotor Blade Airfoils, ASME 2003. Vol. 1252003

[40] Corten GP, Veldkamp HF. Insects cause double stall. In: European Wind Energy Conference. Copenhagen, Denmark; 2001. pp. 470-474

[41] Fuglsang P, Antoniou I, Dahl KS, Aagaard Madsen H. Wind Tunnel Tests of the FFA-W3-241, FFA-W3-301 and NACA 63-430 Airfoils. Denmark: Forskningscenter Risoe. Risoe-R, No. 1041(EN); 1998

[42] Hand MM, Simms DA, Fingersh LJ, Jager DW, Cotrell JR, Schreck S, Larwood SM. Unsteady Aerodynamics Experiment Phase VI: Wind Tunnel Test Configurations and

Available Data Campaigns. National Renewable Energy Laboratory. NREL/TP-500-29955; 2001

[43] Giguère P, Selig MS. Design of a Tapered and Twisted Blade for the NREL Combined Experiment Rotor, Department of Aeronautical and Astronautical Engineering University of Illinois at Urbana-Champaign Urbana, Illinois, NREL. NREL/SR-500-26173; 1999

[44] Schlichting H. Boundary-Layer Theory. 9th ed. New York, USA: Springer; 1979

[45] Breton S-P, Coton FN, Moe G. A study on rotational effects and different stall delay models using a prescribed wake vortex scheme and NREL phase VI experiment data. *Wind Energy*. 2008; 11, 5:459-482

[46] Lindenburt C. Investigation into Rotor Blade Aerodynamics Analysis of the stationary measurements on the UAE phase-VI rotor in the NASA-Ames wind tunnel. ECN-C--03-025; 2003

[47] Kevorkian J, Cole JD. Multiple Scale and Singular Perturbation Methods. Applied Mathematical Sciences. Vol. 114. New York: Springer; 1996

[48] Manwell JF, McGowan JG. Chapter 3. In: *Wind Energy Explained*. 2nd Edition ed. WILEY; 2009

[49] Musial WD, Butterfield CP, Jenks MD. A Comparison of Two- and Three- Dimensional S809 Airfoil Properties for Rough and Smooth HAWT Rotor Operation, 9th ASME Wind Energy Symposium New Orleans, Louisiana, Solar Energy Research Institute (SERI), SERI/TP-257-3603 UC Category: 261 DE89009512